Cement & Concrete Composites 33 (2011) 978–991

Contents lists available at ScienceDirect

Cement & Concrete Composites

journal homepage: www.elsevier.com/locate/cemconcomp

Evaluation of three-dimensional effects in short deep beams using a rigid-body-spring-model

Yasar Hanifi Gedik [a,*], Hikaru Nakamura [a], Yoshihito Yamamoto [b], Minoru Kunieda [a]

[a] Department of Civil Engineering, Nagoya University, Chikusa-ku, Nagoya 464-8603, Japan
[b] Department of Civil & Environmental Engineering, National Defense Academy, 1-10-20 Hashirimizu, Yokosuka, Kanagawa 239-8686, Japan

ARTICLE INFO

Article history:
Received 21 June 2010
Received in revised form 23 June 2011
Accepted 26 June 2011
Available online 6 July 2011

Keywords:
Shear failure
Rigid-body-spring model
Concrete spalling
Strut
Confinement effect

ABSTRACT

Three-dimensional (3-D) effects in short deep beams without stirrups that failed in shear were investigated experimentally and analytically. Two deep beams with a shear span to depth ratio (a/d) of 0.5 and with different beam widths were tested. The effect of beam width on load-carrying capacity, failure mode, crack pattern and 3-D behavior was investigated, and shape effect due to beam width was clarified. In addition, the beams were analyzed by the 3-D rigid-body-spring model (RBSM). RBSM is a discrete form of modeling that presents realistic behavior from cracking to failure, and 3-D RBSM is applicable to simulate 3-D behavior as well as the confinement effect of concrete. Analytical results in terms of load–displacement curves and crack pattern are compared with the experimental results. Three-dimensional deformations, strut widths and cross-sectional stress distribution are investigated analytically and compared with the experimental results to determine 3-D behavior in detail. The 3-D effects in short deep beams are clarified.

© 2011 Elsevier Ltd. All rights reserved.

1. Introduction

Shear failure behavior of RC deep beams is a complex matter that is affected by the compression failure of concrete, shear crack propagation, bond and anchorage of reinforcing bars and a number of other factors. Therefore, modeling shear failure is one of the difficult problems in the numerical simulation of concrete structures. The prediction of damage and failure of concrete, which is a quasi-brittle heterogeneous material, requires a physically realistic and mathematically sound description of softening behavior [1–3]. Since the failure of deep beams localizes near the support and loading points, where there exist complex states of high stress, accurate representation of softening behavior is both essential and complicated. Attempts to describe the failure by local continuum theory have been inadequate since the localization phenomena caused by material softening cannot be obtained objectively [1,3]. Such models tend to exhibit mesh dependency of deformation, local strain, as well as the localization area [4]. On the other hand, numerical methods based on discrete mechanics have been proposed and applied to concrete structures [5–10]. The discrete methods do not rely on the continuum assumption and this facilitates some aspects of fracture modeling. The rigid-body-spring model (RBSM) is one such method, which was first proposed by Kawai [11–14]. RBSM can show realistic behavior from cracking to failure, and it can also be used to investigate stress transfer mechanisms at the meso-level [15,16]. Furthermore, 3-D RBSM is applicable to the simulation of 3-D behavior as well as the effects of confinement of concrete.

Size effect in concrete deep beams has been investigated and presented in the literature by several researchers [17–21]. Walraven and Lehwalter [17] stated that the size effect in short members without shear reinforcement, in which behavior is dominated by strut and tie action, is significant.

In this study, the basic performance of 3-D RBSM developed by Yamamoto et al. [15,16] is presented through simulations of uniaxial tension, uniaxial compression, triaxial compression and confined concrete. Then, the shape effect resulting from beam width in short deep beams is investigated in detail, as well as 3-D behavior using 3-D RBSM. These 3-D effects in short deep beams are important due to lateral deformation, the spalling of concrete on the surface, and the confinement effect in the core cross-sectional area [22]. In our study, two short deep beams having different widths are tested, and the failure mechanism is discussed in order to determine the effect of beam width on behavior. The tested beams are simulated by 3-D RBSM and the results, such as the load–displacement curve, deformation, and failure depths on the strut, are compared. Moreover, the analyses are expanded to include various width cases to clarify the effect of beam width. Furthermore, a beam with shear span to depth ratio $a/d = 1.5$ is analyzed and compared with an $a/d = 0.5$ beam, and a different failure mechanism is presented.

* Corresponding author. Tel.: +81 52 789 4484.
E-mail addresses: hanifigedik@msn.com (Y.H. Gedik), hikaru@civil.nagoyau.ac.jp (H. Nakamura), yyama@nda.ac.jp (Y. Yamamoto), kunieda@civil.nagoyau.ac.jp (M. Kunieda).

0958-9465/$ - see front matter © 2011 Elsevier Ltd. All rights reserved.
doi:10.1016/j.cemconcomp.2011.06.004

2. Analytical model

2.1. 3-D RBSM

In 3-D RBSM, concrete is modeled as an assemblage of rigid particles interconnected by springs along their boundary surfaces (Fig. 1a). The crack pattern is strongly affected by the mesh design as the cracks initiate and propagate through the interface boundaries of particles. Therefore, a random geometry of rigid particles is generated by a Voronoi diagram (Fig. 1b), which reduces mesh bias on the initiation and propagation of potential cracks [12].

The response of the spring model provides an insight into the interaction among the particles, which is different from models based on continuum mechanics. In this model, each rigid particle has three translational and three rotational degrees of freedom defined at the nuclei (or nodal points) that define the particles according to the Voronoi diagram (Fig. 1a). The boundary surface of two particles is divided into several triangles with a center of gravity and vertices of the surface as seen in the figure. One normal and two tangential springs are set at the center of each triangle. By distributing the springs in this way, over the Voronoi facet common to two neighboring nodal points, this model accounts for the effects of bending and torsional moment without the need to set any rotational springs [15,16].

2.2. Concrete material model

The constitutive models for tension, compression and shear that are used in 3-D RBSM are shown in Fig. 2 [15]. The tensile model for normal springs is shown in Fig. 2a. Up to tensile strength, the tensile behavior of concrete is modeled as linear elastic and, after cracking, a bilinear softening branch according to a ¼ model is assumed. In the model, σ_t, g_f and h represent tensile strength, tensile fracture energy, and distance between nuclei, respectively. The model takes into consideration tensile fracture energy.

Fig. 2b shows the stress–strain relation for compression of normal springs that was modeled as an S-shape curve combining two quadratic functions given in Eq. (1). The parameters of ε_{c1}, a_0, b_0, a_1, b_1 and c_1 are calculated by Eq. (2), based on Table 1, in which each parameter has been decided by conducting parametric analyses comparing with the test results of uniaxial tension, uniaxial compression, hydrostatic compression and triaxial compression. The parametric analyses include a variety of specimen size, shape, mesh size and concrete strengths. These parameters are recommended for normal strength concrete. Moreover, the average size of the Voronoi particles (mesh size) to use the parameters was recommended from 10 mm to 30 mm [16]. The applicability of the parameters and concrete model as well as the mesh dependency will be discussed in Section 2.4.

The compression model considers neither softening behavior nor failure of the normal springs. However, compressive failure behavior can be simulated with a confinement effect by means of a combination of a normal spring and a shear spring.

$$\sigma = \begin{cases} a_0\varepsilon^2 + b_0\varepsilon & (\varepsilon > \varepsilon_{c1}) \\ a_1\varepsilon^2 + b_1\varepsilon + c_1 & (\varepsilon \le \varepsilon_{c1}) \end{cases} \tag{1}$$

$$\varepsilon_{c1} = -\frac{2\sigma_c}{E(1+\alpha_{c1})} \tag{2a}$$

$$a_0 = -\frac{E(1-\alpha_{c1})}{2\varepsilon_{c1}} \tag{2b}$$

$$b_0 = E \tag{2c}$$

$$a_1 = \frac{E(\alpha_{c2}-\alpha_{c1})}{2(\varepsilon_{c2}-\varepsilon_{c1})} \tag{2d}$$

$$b_1 = \frac{E(\alpha_{c1}\varepsilon_{c2}-\alpha_{c2}\varepsilon_{c1})}{\varepsilon_{c2}-\varepsilon_{c1}} \tag{2e}$$

$$c_1 = -a_1\varepsilon_{c1}^2 - b_1\varepsilon_{c1} - \sigma_c \tag{2f}$$

The shear stress–strain relation represents the combination of two tangential springs. The combined shear strain is defined by Eq. (3), in which γ_l and γ_m represent the strains of the springs in each direction tangential to the fracture surface [23]. Then, combined shear stress τ is calculated from the shear stress–strain relation, and the shear stresses for each direction (τ_l and τ_m) are distributed by Eq. (4).

$$\gamma = \sqrt{\gamma_l^2 + \gamma_m^2} \tag{3}$$

$$\tau_l = \tau(\gamma_l/\gamma), \quad \tau_m = \tau(\gamma_m/\gamma) \tag{4}$$

Stress–strain relationship for shear is given in Fig. 2c and Eq. (5). In the model, τ_f and γ_f represent shear strength and strain corresponding to strength, respectively. The stress elastically increases up to the shear strength with the slope of shear modulus (G) and softening behavior is also assumed. K is the shear-softening coefficient that is defined by Eq. (6). It is assumed that the shear-softening coefficient K depends upon the stress of the normal spring as represented in Eq. (6) and Fig. 2d, where, β_0, β_{max} and x are the parameters of dependency on the normal spring for the shear-softening coefficient.

$$\tau = \begin{cases} G\gamma & (\gamma < \gamma_f) \\ max\left(\tau_f + K(\gamma-\gamma_f), 0.1\tau_f\right) & (\gamma \ge \gamma_f) \end{cases} \tag{5}$$

$$K = \beta G \tag{6a}$$

$$\beta = min(\beta_0 + \chi(\sigma/\sigma_b), \beta_{max}) \tag{6b}$$

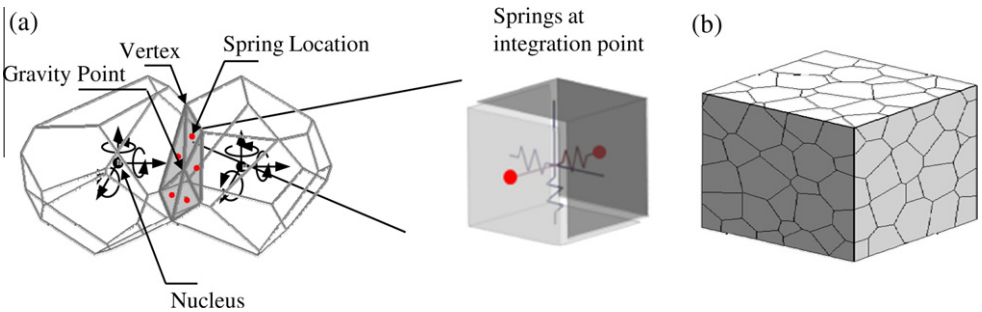

Fig. 1. (a) Rigid-body-spring model and (b) Voronoi diagram.

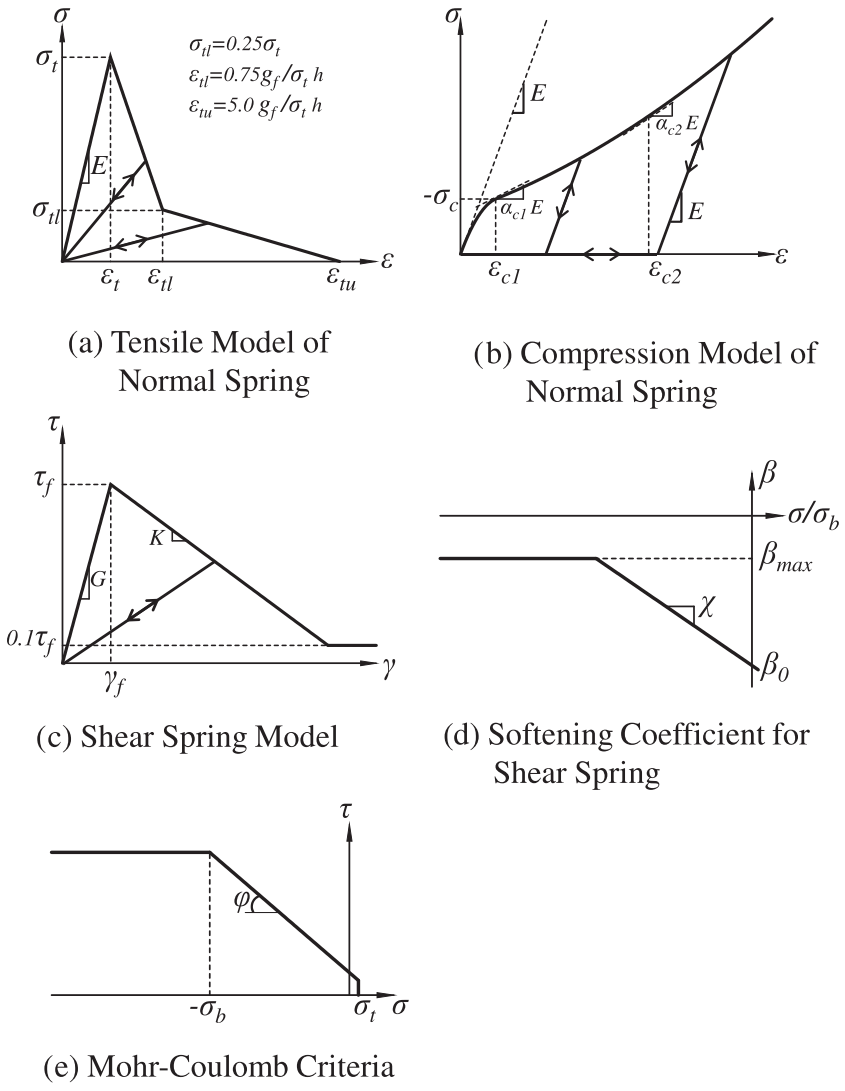

Fig. 2. Constitutive models for concrete [15].

Table 1
Model parameters [16].

Normal spring							Shear spring							
Young modulus	Tensile response		Compressive response				Young modulus	Fracture criterion			Softening Behavior			
E (N/mm^2)	σ_t (N/mm^2)	g_f (N/mm^2)	σ_c (N/mm^2)	ε_{c2}	α_{c1}	α_{c2}	$\eta = G/E$	c (N/mm^2)	φ (degree)	σ_b (N/mm^2)	β_0	β_{max}	χ	κ
$1.4E^*$	$0.80f_t^*$	$0.5G_f*$	$1.5f_c'^*$*	−0.015	0.15	0.25	0.35	$0.14f_c'^*$	37	$f_c'^*$	−0.05	−0.025	−0.01	−0.3

*Indicates test values. E^*: Young modulus, f_t^*: tensile strength, G_f^*: fracture energy, $f_c'^*$: compressive strength.

The Mohr–Coulomb criterion is assumed as the failure criteria for the shear spring (Fig. 2e and Eq. (7)), where c and φ are cohesion and the angle of internal friction, respectively. Shear strength is assumed to be constant when normal stress is greater than σ_b, which is termed the compression limit value [16]. The values of the parameters are given in Table 1.

$$\tau = \begin{cases} c - \sigma \tan \varphi & (\sigma > -\sigma_b) \\ c + \sigma_b \tan \varphi & (\sigma \leqslant -\sigma_b) \end{cases} \tag{7}$$

Moreover, it is assumed that shear stress decreases with an increase in crack width at the cracked surface, in which tensile softening occurs in a normal spring by taken into consideration the shear deterioration coefficient β_{cr} as represented in Eq. (8), which is similar to Saito's model [14,24]. Here, ε_t and ε_{tu} are cracking strain and ultimate strain in a normal spring, respectively. The unloading and reloading paths of the shear springs are directed through the origin.

$$\tau = \begin{cases} \beta_{cr} G\gamma \\ \beta_{cr} max\left(\tau_{ft} + K(\gamma_{max} - \gamma_{ft}), 0.1\tau_{ft}\right) \end{cases} \tag{8a}$$

$$\beta_{cr} = \frac{\varepsilon_t}{\varepsilon} exp\left\{\frac{k}{\varepsilon_{tu}}(\varepsilon - \varepsilon_t)\right\}^{(\gamma<\gamma_{ft})}_{(\gamma\geqslant\gamma_{ft})} \tag{8b}$$

$$\tau_{ft} = c - \sigma_t \tan \varphi \tag{8c}$$

2.3. Reinforcement model

Reinforcement is modeled as a series of regular beam elements (Fig. 3) that can be freely located within the structure, regardless of the concrete mesh design [13]. Three translational and three rotational degrees of freedom are defined at each beam node. The reinforcement is attached to the concrete particles by means of zero-size link elements that provide a load-transfer mechanism between the beam node and the concrete particles [14].

The stress–strain relation of reinforcement is defined by a bilinear model. Crack development is strongly affected by the bond interaction between concrete and reinforcement. The bond stress–slip relation is provided in the spring parallel to the reinforcement of linked element. Fig. 4 shows the relation that is defined by Eq. (9) up to peak strength [25], and the curve proposed by CEB-FIB is assumed after peak strength [26].

$$\tau = 0.36 f_c'^{2/3}\left\{1 - exp\left(-40(s/D)^{0.5}\right)\right\} \quad (9)$$

where D is diameter of the reinforcement and s represents slippage.

2.4. Applicability of the model

2.4.1. Uniaxial tension

The direct uniaxial tension experiment with notched prism specimen carried out by Cornelissen et al. [27] was simulated by 3-D RBSM [16]. Fig. 5a shows the outline of the specimen. The notches with 5 mm width and 5 mm depth were located on the both sides at the middle height of the specimen. In the experiment, the strain was measured also in softening region by extensometers with 35 mm length attached on the specimen, as shown in Fig. 5a. The values of the Young's modulus, the tensile strength and the fracture energy in the experiment were 39,270 N/mm^2, 3.2 N/mm^2 and 103.1 N/m, respectively [27].

The analytical model of the specimen is given in Fig. 5b where the discrete beam elements were employed for modeling the extensometers, in which stiffness of the beam element was set to relatively small value to prevent the effect of the element on the behavior of concrete. The load was applied to both ends of the specimen with displacement control. In order to achieve that, two rigid plate elements were attached on the top and the bottom of the specimens. The thickness of the rigid elements was 20 mm and all degrees of freedom were fixed.

Fig. 6a shows the comparison of the stress and the extension of the extensometer relationship between the analysis and the experimental results. As seen in the figure, a significantly good agreement is obtained for the tensile strength as well as the softening behavior. The simulated failure pattern is given in Fig. 6b. It is observed that the fracture surface is irregular rather than planar due to the Voronoi mesh design.

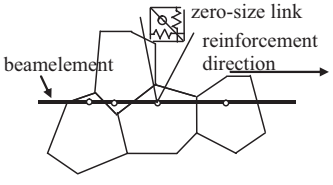

Fig. 3. Reinforcement arrangement (2-D case shown).

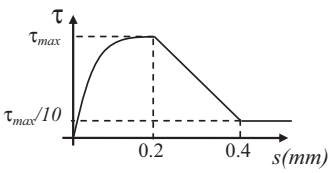

Fig. 4. Bond stress–slip relation.

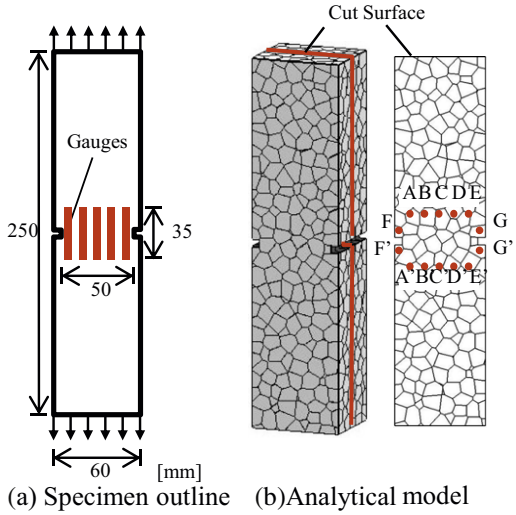

Fig. 5. Specimen layout and its modeling [16].

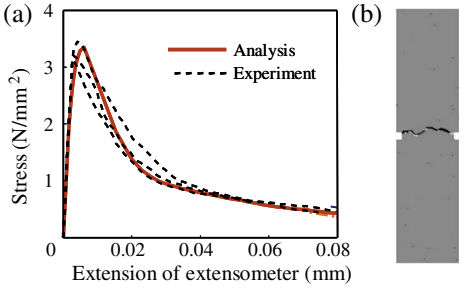

Fig. 6. (a) Stress-extension of the extensometer relationship and (b) deformed shape [16,27].

2.4.2. Uniaxial compression and mesh dependency

3-D RBSM analysis of uniaxial compression test (for a specimen with 100 mm diameter and 400 mm height) carried out by Fujikake et al. [28] was introduced in Yamamoto et al. [15]. Fig. 7a shows a comparison of load–displacement curves between the analysis and the experimental result. As seen in the figure, a reasonably good agreement is obtained. The experimental axial strain distribution and crack pattern are given in Fig. 7b and c shows the simulation results of axial strain, damage pattern of normal springs and 3-D deformed shape. As seen in the figures, the length of fracture region is almost the same for the experiment and the analysis. These results confirm that the analytical model is applicable to simulate stress–strain relationship and fracture region for uniaxial compression [15].

To investigate mesh dependency of the model, the same specimen was also simulated with different mesh geometry and mesh size and the analytical responses were compared [15]. Nine analytical models were prepared having three different mesh size groups of 10 mm (h10), 20 mm (h20) and 30 mm (h30). Each group has three analytical models with different random mesh geometry. Stress–strain relationships for each group are given in Fig. 8a–c. In the figures, each curve represents a different mesh geometry. The curves are almost the same in the pre- and post-peak regions

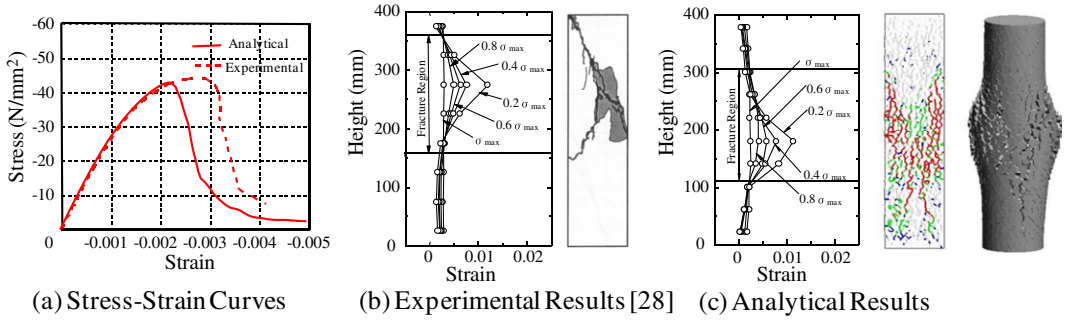

Fig. 7. Comparison of experimental and analytical results [15,28].

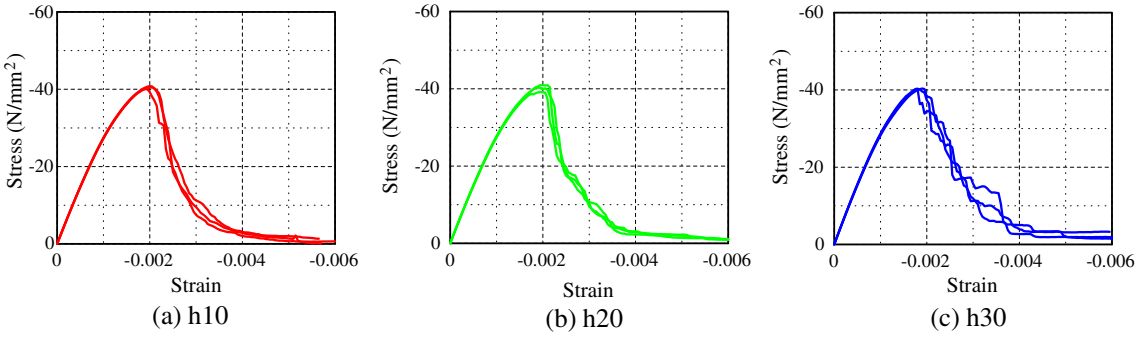

Fig. 8. Mesh sensitivity of stress–strain curve [15].

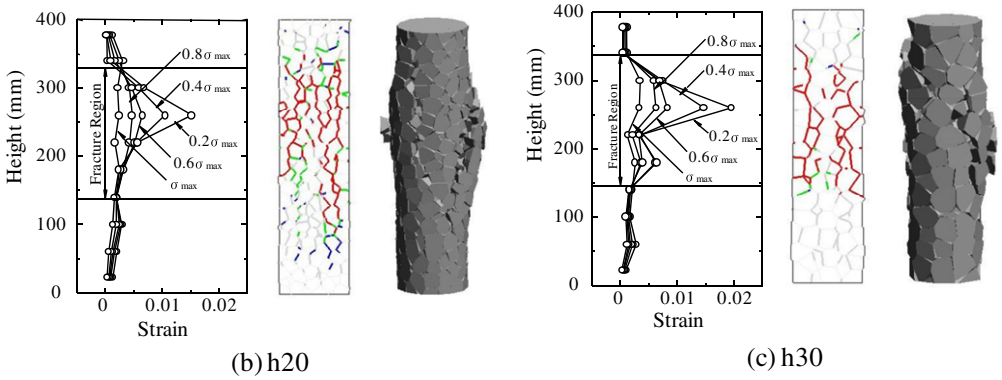

Fig. 9. Mesh sensitivity of fracture behavior [15].

for all mesh sizes and geometries. Fig. 9 shows the analytical results of axial strain, damage pattern of normal spring and 3-D deformed shape due to mesh size. It is obviously shown that localization behavior can be evaluated by the analytical model. It is confirmed that the mesh dependency is not significant as long as the mesh size is between 10 mm and 30 mm.

2.4.3. Triaxial compression

The applicability of 3-D RBSM under a triaxial stress state was confirmed by simulating the experiment of Kotsovos and Newman [15,29]. Fig. 10 shows 3-D RBSM analysis of compression of a cylinder having a diameter of 100 mm and a height of 250 mm. An analytical model of the cylinder is shown in Fig. 10a. Fig. 10b shows a comparison of the axial stress–axial strain and the axial stress–lateral strain relation under various lateral pressures. The experimental and analytical stress–strain curves and maximum stress values agree significantly well. Only for the high confinement of 70 MPa, the analytical stress–strain curves show strain hardening as opposed to the experiments. However, the maximum stress agreed with the experiments. The results show that the dilatancy and confinement effect can be simulated by the 3-D RBSM. Therefore, the compressive failure simulation capability of the concrete material model in a 3-D RBSM is confirmed.

2.4.4. Confined concrete

The uniaxial compression test of confined concrete carried out by Akiyama et al. [30] was simulated by 3-D RBSM in order to verify the simulation capability of the confinement effect [16]. The analytical model is shown in Fig. 11, which consists of Voronoi mesh design, modeling of stirrups and a cross section of a rebar. The stirrups were modeled by beam elements, of which the cross section was divided into small segments as shown and then the

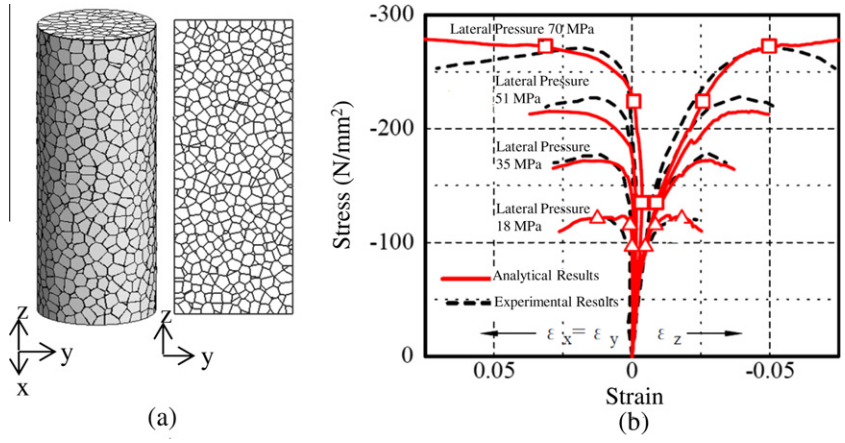

Fig. 10. Comparison of experimental results (f'_c = 46.9 MPa, [29]) and 3-D RBSM: (a) analytical model; (b) stress–strain relation [15].

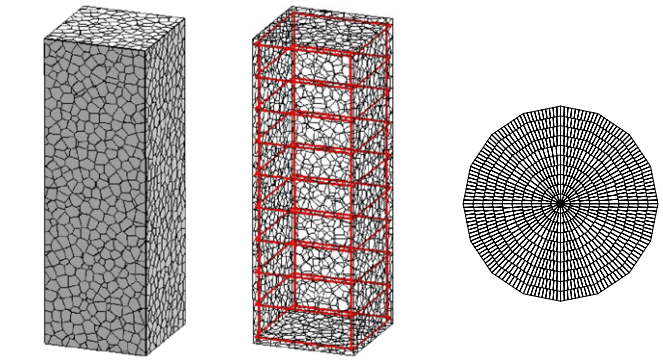

Fig. 11. Analytical model [16].

Table 2
Stirrup properties [16].

Specimen No.	Properties of stirrup			
	Diameter (mm)	Spacing (mm)	Volumetric ratio (%)	Yield strength (MPa)
SF1P1Y3	6.4	25	1.92	1288
SF1P2Y1	6.0	50	1.01	317
SF1P2Y3	6.4	50	0.96	1288
SF1P3Y1	6.0	100	0.51	317
SF1P3Y2	6.0	100	0.51	1028
SF1P3Y3	6.4	100	0.48	1288
SF1P4Y3	6.4	150	0.32	1288

stress was calculated for each segment. Therefore, the local inelasticity and the bending effect of the rebar were considered. Table 2 shows the specimen properties. Various values of volumetric ratio and yield strength of reinforcement were considered.

Fig. 12 shows the comparison of stress–strain relationship for each specimen between the analysis and the experimental result. As seen in the figures, a significantly good agreement is obtained for the compressive strength of confined concrete as well as the post peak behavior. This tends to confirm the simulation capability of the model for various confinement conditions.

3. Simulation of deep beam with a/d = 0.5

3.1. Comparison of analytical and experimental results

The details of the tested specimens and experimental results are introduced in Appendix A. The tested BS4bw100 and BS4bw200 beams are simulated by 3-D RBSM and the load–displacement curves and crack patterns are compared. The average size of the Voronoi particles in the analysis was 22 mm for each case.

The load–displacement curves of the experimental results and analysis for BS4bw100 are compared in Fig. 13. The analytical peak load is 638 kN, which is lower than the experimental result of 751 kN. The comparison of crack patterns at the analytical pre-peak load P = 452 kN (labeled 'a' in Fig. 13) and at the peak load (b) are shown in Fig. 14. The analytical deformed shapes are magnified by a factor of 60. Reasonable agreement between analysis and the experimental results is observed. However, the damage mainly localizes only one side of the beam in the experiment. On the other hand, the damage is distributed on both sides of the beam in the analysis since the specimen is homogeneous. Therefore, more energy is absorbed in the analysis, which is one possible reason for lack of brittle sudden failure in the analysis, as distinct from the experiment (see Fig. 13).

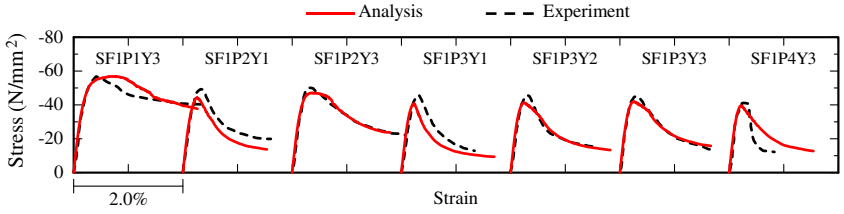

Fig. 12. Stress–strain relationships for different confinement conditions [16,30].

The comparison of the load–displacement curves for BS4bw200 is also given in Fig. 13. The analytical peak load is 1513 kN, which is slightly lower than the experimental result, which is 1568 kN. The curves show reasonably good agreement in both the pre-peak and post-peak regions. The comparison of crack patterns at the analytical pre-peak load $P = 1028$ kN (A) and at the peak load (B) are shown in Fig. 15. The analytical deformed shapes are magnified by a factor of 60. Reasonable agreement between analysis and the experimental results is observed.

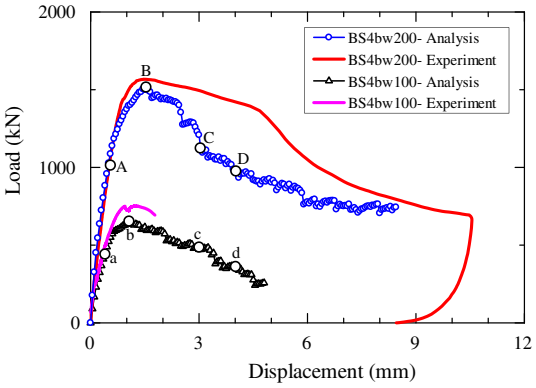

Fig. 13. Load–displacement curves.

3.2. 3-D deformed shapes

A failure mechanism can be investigated in detail by the 3-D-RBSM as it provides the 3-D deformed shape. Figs. 16 and 17 show 3-D deformed shapes at the peak and post-peak loads for BS4bw100 and BS4bw200, respectively. To indicate the failure behavior clearly, the deformed shapes are magnified by a factor of 20.

At peak load, no significant lateral deformation is observed along the compression strut for either of the cases (b, B). The lateral deformation is formed after peak load (c, C) and it increases with further post-peak loading (d, D) as shown in the figures. The lateral deformation behavior appears to be similar for each case, judging by a comparison of the figures from peak load to post-peak loads. The large lateral deformation in the post-peak region is in agreement with the spalling behavior in the experiment. Moreover, relative lateral deformation is significantly higher in the case of

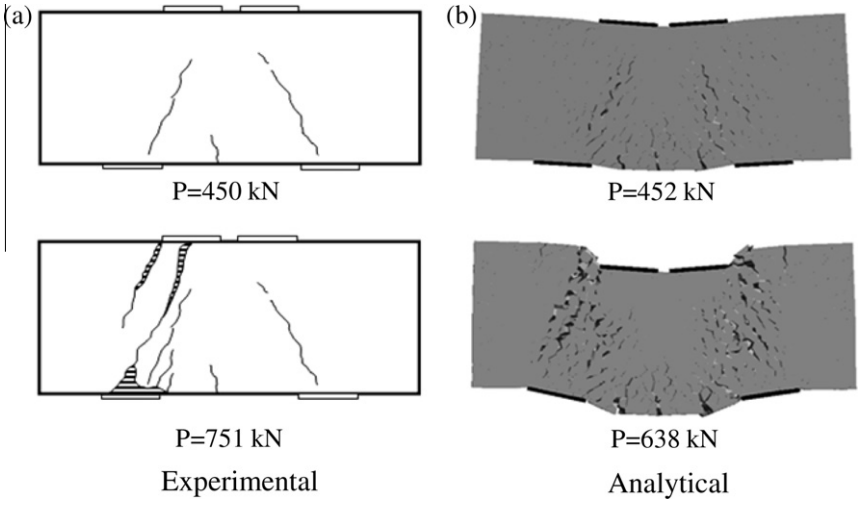

Fig. 14. Crack patterns (BS4bw100 specimen).

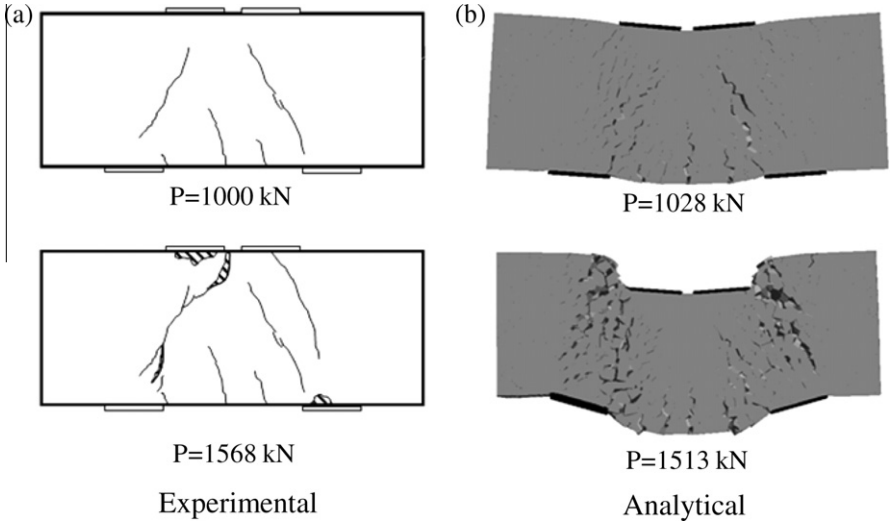

Fig. 15. Crack patterns (BS4bw200 specimen).

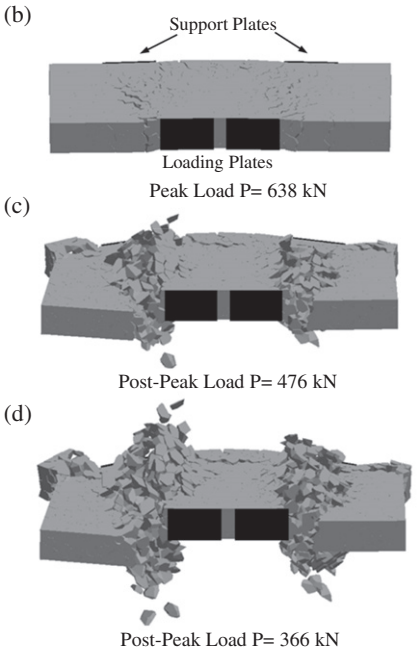

Fig. 16. 3-D deformed shapes of BS4bw100.

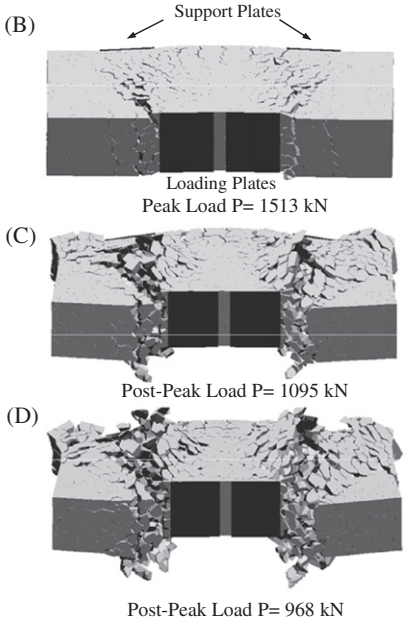

Fig. 17. 3-D deformed shapes of BS4bw200.

BS4bw100, which is similar to the experimental results. Therefore, 3-D behavior is important in understanding the post-peak behavior of RC short deep beams, and the 3-D RBSM can show this behavior realistically.

3.3. Compression Strut

The principal stress distribution on the longitudinal middle section of BS4bw200 is shown in Fig. 18. The maximum stress range is set to 19.50 MPa, which is the compressive strength of concrete

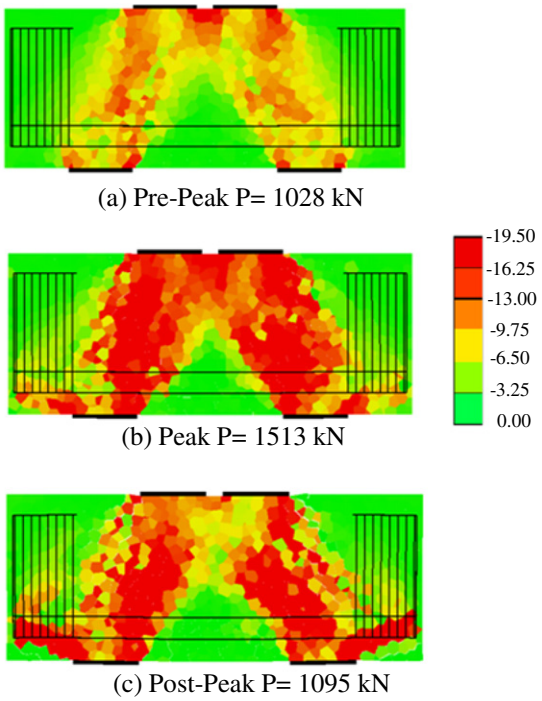

Fig. 18. Principal stress distributions on the longitudinal middle section (stress values are indicated in MPa).

(f'_c). Fig. 18a shows the principal stress distribution at pre-peak load $P = 1028$ kN (A). The strut initiation is shown in the figure. Fig. 18b shows the principal stress distribution at the peak load (B). The strut can be seen clearly in the figure. At post-peak load $P = 1095$ kN (C), the stress decreases near the loading plates, where it remains similar near middle height of the beam and support plates (Fig. 18c).

In order to discuss the 3-D effect in short deep beams, strut widths along the strut are compared using Fig. 18. The strut is determined by the area where the stress is greater than 0.5 f'_c and the measured widths are normalized by plate width. The widths are measured near the loading point (Point1), the middle height of the beam (Point 2), and the support point (Point 3) shown in Fig. 19a. A comparison of normalized strut widths at Points 1, 2 and 3 is given in Fig. 19b. The widths are measured on both the surface and middle longitudinal sections.

In the pre-peak region, the widths increase in all cases. Near the peak load, the strut width at Point 2 is about 1.5 times the plate width on the middle section, while it is smaller than the plate width on the surface section. At Points 1 and 3, the widths on the surface section reach the plate width near the peak load. On the middle section, the strut widths are less than the plate width.

On the surface section, the strut disappears just after the peak load, and no post-peak region is observed due to spalling of concrete on the surface. On the other hand, the strut on the middle section is observed in further post-peak loading because of the confining effect in the middle of the beam. At Points 1 and 2 on the middle, the widths decrease in a similar way as with the load–displacement curve in the post peak, where the strut is almost constant at Point 3. The results show the reason for the different behavior between surface and middle sections is the confining effect in the middle part of the beam after concrete spalling on the surface.

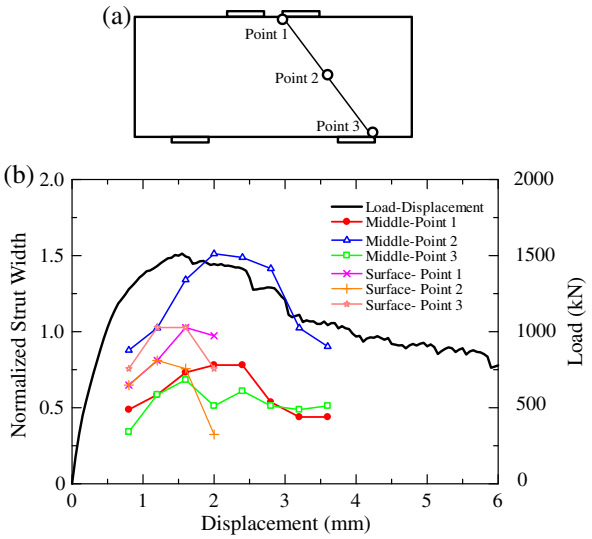

Fig. 19. (a) Strut measurement points and (b) comparison of strut widths.

4. Shape effect due to beam width

4.1. Experimental

In order to investigate the effect of beam width, the experimental results of BS4bw100 and BS4bw200 specimens are compared. Fig. 20 shows the comparison of nominal shear stress for the specimens. As seen in the figure, there is no effect from beam width in the pre-peak region. The maximum shear stress is slightly higher for BS4bw200. On the contrary, the post-peak behavior is different.

Fig. 21 shows the final deformed shape of BS4bw100. The beam failed suddenly under shear compression as a result of excessive lateral deformation and spalling of concrete on the surface. The lateral deformation was observed only on one of the compression strut of the beam. On the other hand, the beam with the larger width (BS4bw200) shows softening behavior in the post-peak region as seen in Fig. 20. The final deformed shape of the beam is shown in Fig. 22. Lateral deformation and spalling of concrete formed along the strut surface. The beam continued to carry the load as there was sufficient interior concrete, as opposed to the case for BS4bw100. Moreover, the lateral deformation occurred on two of the compression strut of the beam in the early post-peak region, which is another reason for softening behavior. However, the damage was localized only on one side of the beam in further post-peak loading. This behavior is confirmed by the change of slope after a mid-span displacement of about 5 mm in the softening part (see Fig. 20).

The comparison of the relative failure depths along the beam width on the failed beams is shown in Fig. 23. The sum of the depth measured on the two surfaces of the strut is taken into account and it is given as a percentage relative to the beam width. The depth near the loading point in the narrower beam extends to 74% of the beam width as seen in the figure, whereas it is only 27% in the wider beam. It is clearly understood that sudden failure occurred in BS4bw100 as the remaining interior concrete near the loading point was relatively small to carry the load toward to the strut, after the large amount of concrete spalling. Otherwise, the load could have been transmitted from loading points to the support in the post-peak region of BS4bw200 as there was sufficient remaining interior concrete and, therefore, ductile behavior was observed. In the figure, the absolute failure depths are given within the parentheses on the points in the figure. The remaining thicknesses of the BS4bw100 beam are only 26 mm, 40 mm and

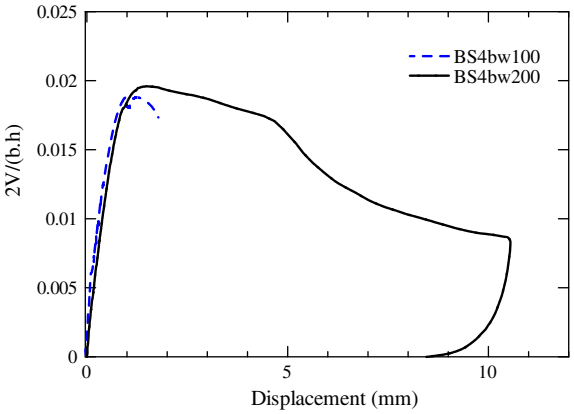

Fig. 20. Nominal shear stress.

Fig. 21. Failure of BS4bw100.

Fig. 22. Failure of BS4bw200.

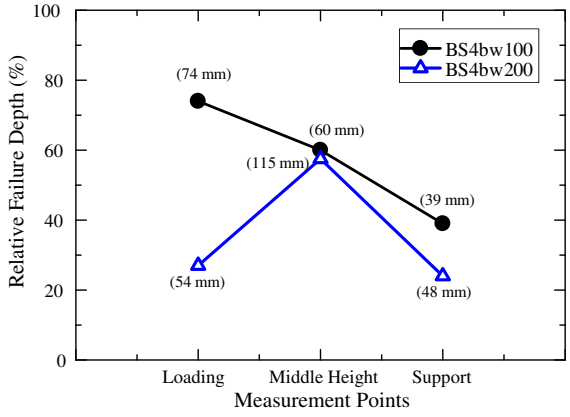

Fig. 23. Comparison of relative failure depths.

Table 3
Properties of test specimens.

Specimen	Beam length L (mm)	Overall height h (mm)	Effective depth d (mm)	Beam width b (mm)	Shear span a (mm)	a/d	Plate width (mm)	Longitudinal reinforcement A_s (mm^2)	ρ_s (%)	f'_c (MPa)
BS4bw300	1000	400	320	300	160	0.5	160	2479	2.58	20.0
BS4bw400	1000	400	320	400	160	0.5	160	3306	2.58	20.0

61 mm near the loading point, middle height of the strut, and support point, respectively, while 146 mm, 85 mm and 152 mm values were recorded for the BS4bw200 beam. The reason for sudden failure can be clearly understood through this comparison, that is, the remaining thickness, especially near the loading point, is too small to carry the load after the peak in BS4bw100. On the other hand, it was significantly higher in the BS4bw200 beam, which could transmit the load from the loading points to support along the strut.

4.2. Analytical

In this section, the effect of beam width on short deep beam behavior is analytically investigated. In addition to the BS4bw100 and BS4bw200 specimens, the analyses are extended to specimens having larger beam widths of 300 mm and 400 mm given in Table 3 in order to clarify the effect of beam width. The length and the height of specimens are the same for all cases; only the widths are different, that is: 100 mm, 200 mm, 300 mm and 400 mm.

Fig. 24 shows a comparison of nominal shear stress as it depends on beam width. The shear stress increases with the increase in beam width. Moreover, more ductile behavior in the post-peak region is observed in the case of larger beam widths, as shown in the figure. The results agree with the observations from the experiments.

The principal stress distribution of the cross-sectional area at the middle of the shear span is shown in Fig. 25. The maximum compressive stress range is set to 40 MPa. The stress is measured at mid-span displacement values of 1 mm, 3 mm and 4.5 mm. In the case of $b = 100$, no stress concentration is observed after the peak load. The result agreed with the experimental results, in which a large amount of lateral deformation was observed and no interior concrete remained. Therefore, sudden failure occurred just after peak load was reached.

On the other hand, in the $b = 200$ case, the stress near the surface decreases due to spalling of concrete and stress concentration occurs at post-peak ($d = 3.0$ mm) on the core concrete and then it decreases at post-peak ($d = 4.5$ mm), where the maximum stress on the cross-section is 43 MPa, which is 2.2 times greater than f'_c. Other than that, the stress concentration in the case of $b = 300$ and 400 is observed both at post-peak ($d = 3.0$ mm) and at post-peak ($d = 4.5$ mm). The maximum stress at $d = 4.5$ mm is 55 MPa ($2.75f'_c$) and 63 MPa ($3.15f'_c$) for the $b = 300$ and 400 mm cases, respectively. The higher maximum stress is induced due to confinement effect in core concrete for the larger beam widths. Therefore, the 3-D stress state in concrete is dominant for larger widths.

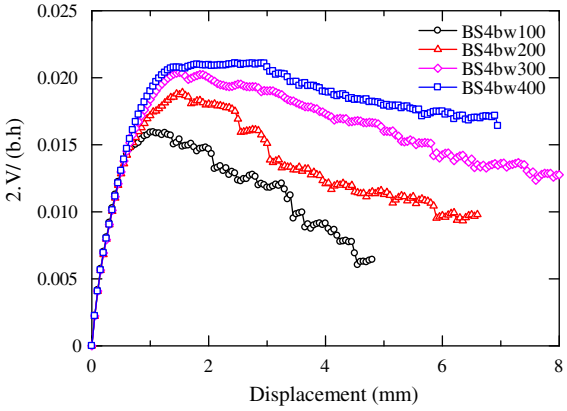

Fig. 24. Nominal shear stress for different beam widths.

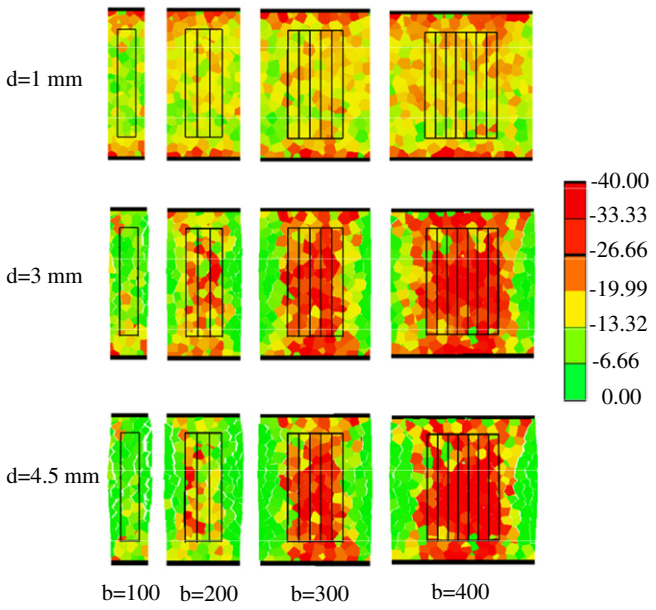

Fig. 25. Principal stress distribution on cross-sectional area (stress values are indicated in MPa).

The stress release area near the surface increases on the middle-height of the beam and it decreases near the loading and support points. The tendency agrees with the absolute failure depth of the experimental result of BS4bw200 (see Fig. 23). The depths of the stress release area are almost similar with the different widths. Therefore, the relative failure depth decreases by the increase of beam width, which leads to more ductile behavior for higher beam widths. Thus, the effect of beam width in short deep beams is clearly understood. Namely, a large amount of spalling occurs in the case of smaller beam widths that may cause sudden failure due to a lack of interior concrete remaining in place. On the other hand, interior concrete is still available to resist the loads in the post-peak region due to the confinement effect in the case of larger beam widths.

5. Simulation of deep beam with $a/d = 1.5$

A beam with $a/d = 1.5$ is analyzed by the 3-D RBSM to investigate 3-D behavior and to make a comparison with the $a/d = 0.5$ case. The specimen details are shown in Table 4 and Fig. 26. The specimen was designed with the same cross-sectional area and the same material properties as BS4bw200 to obtain the effect of shear span to depth ratio on 3-D behavior.

Table 4
Properties of test specimen.

Specimen	Beam length L (mm)	Overall height h (mm)	Effective depth d (mm)	Beam width b (mm)	Shear span a (mm)	a/d	Plate width (mm)	Longitudinal reinforcement A_s (mm^2)	ρ_s (%)	f'_c (MPa)
BS-SR1.5	1640	400	320	200	480	1.5	160	1653	2.58	19.5

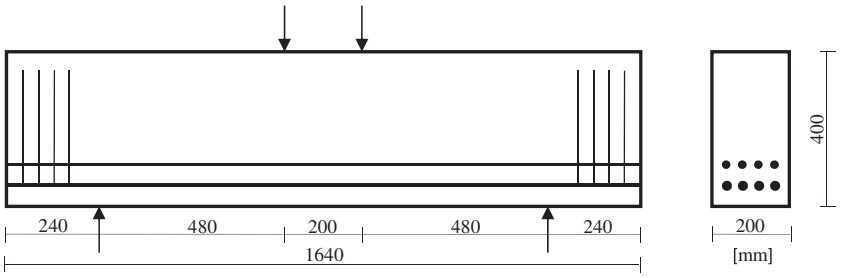

Fig. 26. Specimen layout.

The load–displacement curve is shown in Fig. 27, in which the peak load is 563 kN. Fig. 28 shows the 2-D crack pattern at a magnification factor of 60 until peak load. First, flexural cracks occurred in the beam span. Then, the initial diagonal shear crack was formed, running from near the support plate to the upper part of the strut (A). Afterwards, several shear cracks parallel to first one appeared and developed. Finally, a shear crack running from the outer side of the loading plate formed, and then the beam failed under shear (B).

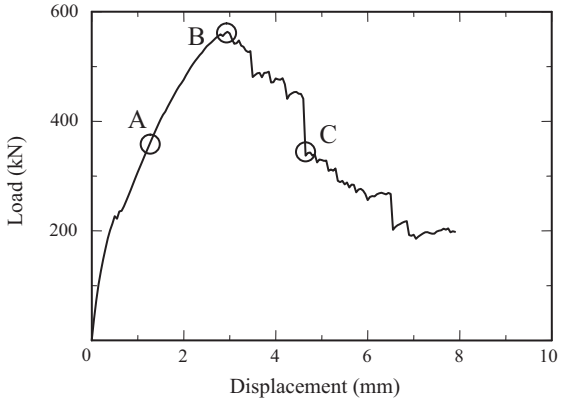

Fig. 27. Load displacement curve.

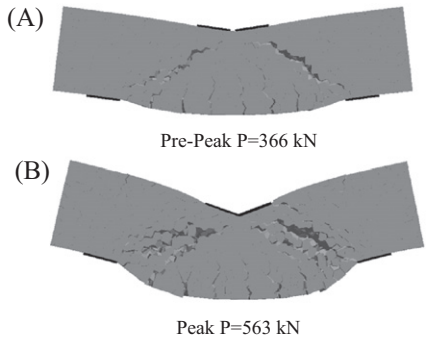

Fig. 28. Elevation view of deformed shapes.

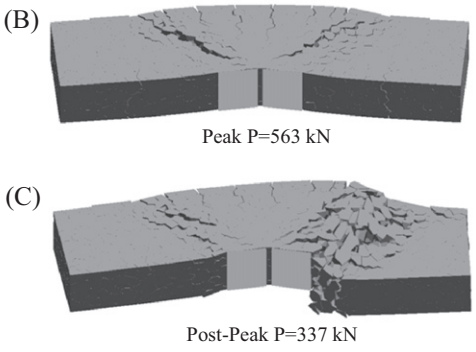

Fig. 29. 3-D view of deformed Shapes.

Fig. 29 shows the three-dimensional deformed shapes of the beam at a peak load $P = 563$ kN (B) and a post-peak load $P = 337$ kN (C). The deformed shapes are magnified by a factor of 25 in order to show the behavior clearly. The difference in 3-D behavior compared with the case of $a/d = 0.5$ is obvious. That is, the lateral deformation is not dominant in this case as seen in the figure.

The different behavior between the $a/d = 0.5$ and 1.5 cases are clear. In the case of $a/d = 0.5$, the stress flows along the strut from the loading points to the support points based on the tied-strut mechanism. Therefore, spalling of concrete and lateral deformation is observed due to high compression. On the other hand, both arch action and flexural behavior occur in the case of $a/d = 1.5$. Thus, the strut mechanism is less effective compared with the $a/d = 0.5$ case, and lateral deformation is not dominant.

6. Summary and conclusions

In this study, the simulation tool used is the 3-D RBSM, which is a form of discrete modeling that presents realistic behavior from cracking to failure. 3-D RBSM is applicable to simulate 3-D behavior as well as the confinement effect of concrete. RBSM can also be used to investigate the stress-transfer mechanism at the meso levels.

To investigate the applicability of the model, uniaxial tension and compression cylinder and a confined concrete specimen are

Table A1
Properties of test specimens.

Specimen	Beam length L (mm)	Overall height h (mm)	Effective depth d (mm)	Beam width b (mm)	Shear span a (mm)	a/d	Plate width (mm)	Longitudinal reinforcement A_s (mm^2)	ρ_s (%)	Compressive strength f'_c (MPa)	Tensile strength f_t (MPa)	Elastic modulus E (GPa)
BS4bw100	1000	400	320	100	160	0.5	160	826 (2D13 + 2D19)	2.58	20.1	1.70	23.1
BS4bw200	1000	400	320	200	160	0.5	160	1653(4D13 + 4D19)	2.58	19.5	1.67	22.8

simulated. Good agreement between the experimental and analytical results is obtained in terms of load–displacement curves, 3-D deformed shapes, and axial strain values. Therefore, the applicability of the analytical model has been confirmed.

Two beams with $a/d = 0.5$ and different widths were tested to investigate 3-D effects in short deep beams. Sudden failure occurred in the smaller width beam due to the relatively large amount of concrete spalling, and more ductile behavior was obtained in wider beam. The effect of beam width on the behavior of short deep beams is observed clearly.

The tested beams are simulated by the 3-D RBSM, and the results in terms of load–displacement curve and crack pattern agree reasonably well with the experimental results. Furthermore, 3-D deformations as well as the strut width on the surface and middle longitudinal sections are investigated. The importance of the 3-D effects resulting from the spalling of concrete on the surface, and the confinement effects in the middle section is confirmed.

The effect of beam width in short deep beams is investigated analytically by comparing four beams having widths of 100 mm, 200 mm, 300 mm and 400 mm. As with the experiments, more ductile behavior is observed as a result of the increase in beam width. Moreover, the effect of beam width, spalling behavior on the surface, and the confinement effect in the middle section are clarified by 3-D RBSM. The ductile behavior resulting from the increase in beam width is caused by the difference of the core concrete width and the confinement effect of the core concrete.

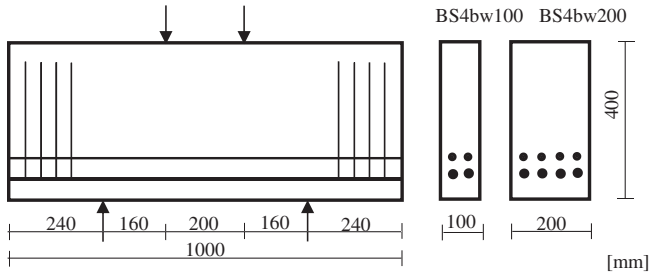

Fig. A1. Specimen layouts.

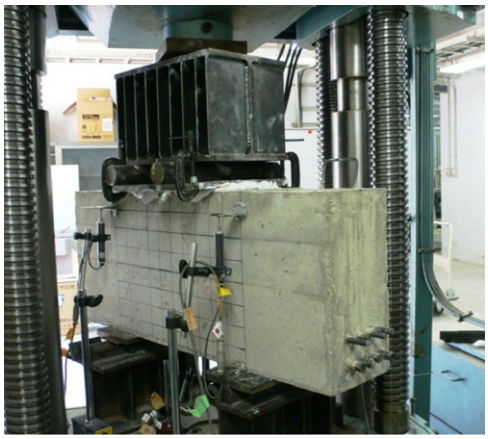

Fig. A2. Experimental setup.

Appendix A

A.1. Tested specimens and experimental details

Two specimens as described in Table A1 were tested in order to investigate the 3-D effects in short deep beams with $a/d = 0.5$ and without stirrups in the shear spans. Fig. A1 shows the dimensions

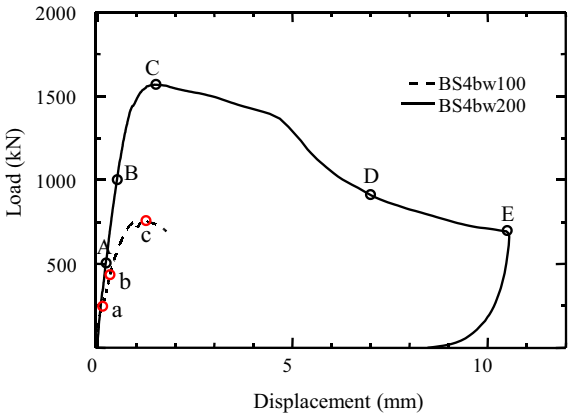

Fig. A3. Load–displacement curves.

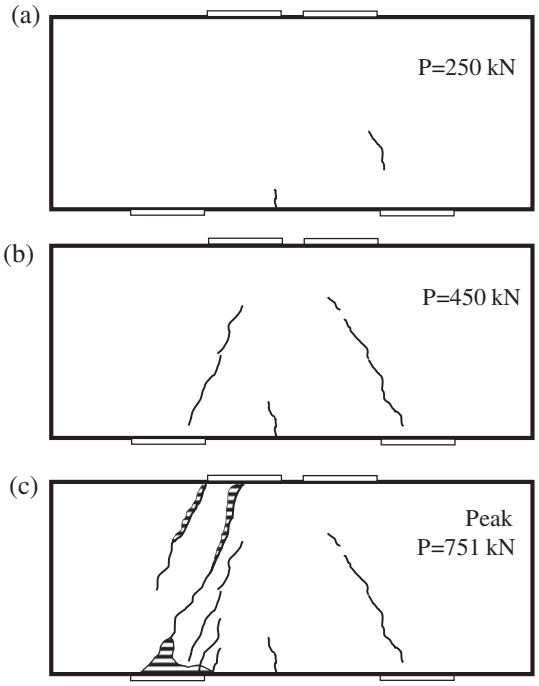

Fig. A4. Crack patterns (specimen BS4bw100).

of the tested specimens. The beam length and height of the beams are the same in both cases, while the beam widths are different as indicated. The longitudinal reinforcement ratio was kept constant in each case. Relatively large plate widths were used to prevent bearing failure on the loading point.

Fig. A2 shows the experimental setup for four-point loading that was applied to the test specimens. The load was distributed on the loading points using a steel beam. Steel rollers were used between the loading plates and the steel beam. 4 LVDT for support deflections and 1 LVDT for mid-span deflection were used to obtain the beam displacements. The relative mid-span deflection was taken into consideration by subtracting the support displacements.

A.2. Experimental results

A.2.1. Deep beam BS4bw100

The load–displacement curve of the BS4bw100 specimen is shown by the dashed line in Fig. A5. The peak load is 751 kN. Sudden shear failure occurred and no post-peak region was measured, as shown in the figure.

Fig. A4 shows the crack pattern of the beam up until peak load. The first shear crack was formed in the lower part of the strut together with a mid-span bending crack at $P = 250$ kN (a). At $P = 450$ kN, shear cracking was propagated and another shear crack occurred on the other side (b). At peak load (c), two shear cracks, one from the outer side of the loading plate, and another running from the support to the loading point, developed and the beam suddenly failed in shear-compression failure with spalling of the concrete, indicated by the shaded areas.

A.2.2. Deep beam BS4bw200

The load–displacement curve of the BS4bw200 specimen is shown by the solid line in Fig. A3.The peak load is 1568 kN and ductile softening behavior can be observed in the post-peak region.

Fig. A5 shows the crack pattern of the beam up until peak load. The first shear crack developed from the support to the upper part of the strut at $P = 500$ kN (A). Then, another shear crack occurred on the other side together with mid-span bending cracks at $P = 1000$ kN (B). At peak load, new shear cracks were developed that connected to the loading plates and led to shear compression failure with spalling of the concrete (C). In the post-peak region, the spalling of concrete and lateral deformation increased (D) and developed along the entire strut (E) as shown in the figures.

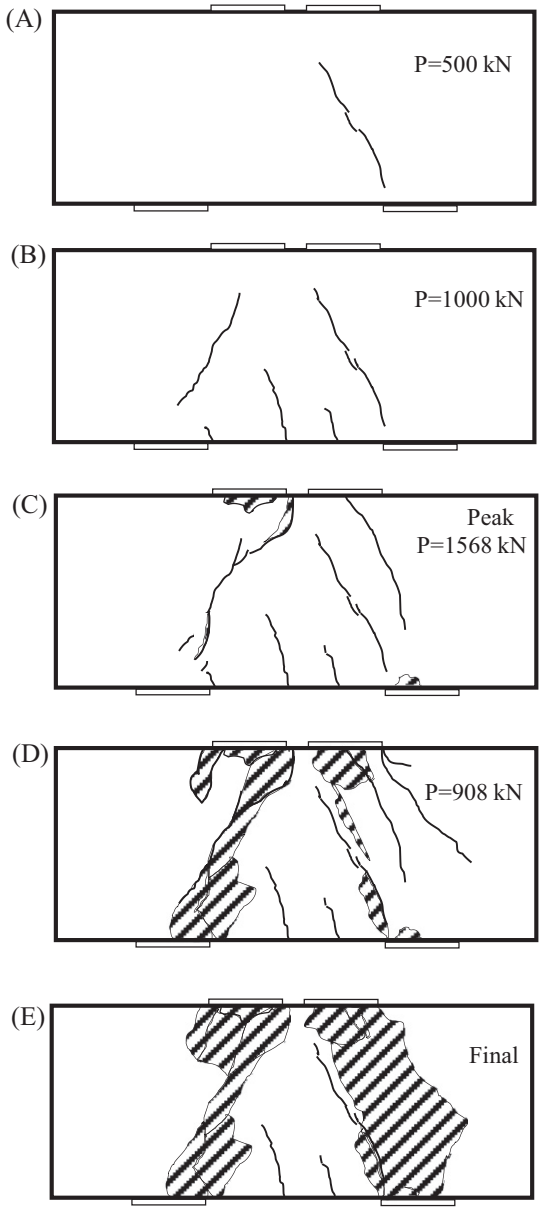

Fig. A5. BS4bw200 crack patterns.

References

[1] Bazant ZP. Mechanics of distributed cracking. Appl Mech Rev, ASME 1986;39(5):675–705.
[2] Mazars J, Pijaudier-Cabot G. Continuum damage theory: application to concrete. Internal report 71, LMT, Cachan; 1986.
[3] Bazant ZP, Pijaudier-Cabot G. Nonlocal continuum damage, localization instability and convergence. J Appl Mech 1988;55:287–93.
[4] Bazant ZP. Instability, ductility, and size effect in strain softening solids. J Engng Mech Div, ASCE 1976;102:331–44.
[5] Meguro K, Hakuno M. Fracture analysis of concrete structures by the modified distinct element method. Struct Eng/Earthquake Eng 1989;6(2):283–94.
[6] Shi GH, Goodman RE. Generalization of two-dimensional discontinuous deformation analysis for forward modelling. Int J Numer Anal Meth Geomech 1989;13:359–80.
[7] Schlangen E. Experimental and numerical analysis of fracture process in concrete. PhD thesis, Delft University of Technology, Netherlands, 1993.
[8] Schlangen E, van Mier JGM. Experimental and numerical analysis of micromechanisms of fracture of cement-based composites. Cem Concr Compos 1992;14:105–18.
[9] Bolander JE, Shiraishi T, Isogawa Y. An adaptive procedure for fracture simulation in extensive lattice networks. Eng Fract Mech 1996;54:325–34.
[10] Van Mier JGM. Fracture processes of concrete: assessment of material parameters for fracture models. Boca Raton, Florida: CRC Press, Inc.; 1997.
[11] Kawai T. New discrete models and their application to seismic response analysis of structures. Nucl Eng Des 1978;48:207–29.
[12] Bolander JE, Hong GS, Yoshitake K. Structural concrete analysis using rigid-body-spring networks. Comput-Aided Civil Infrastruct Eng 2000;15:120–33.
[13] Bolander JE, Hong GS. Rigid-body-spring network modeling of prestressed concrete members. ACI Struct J 2002;99(5):595–604.
[14] Saito S. Fracture analyses of structural concrete using spring networks with random geometry. PhD thesis. Fukuoka, Kyushu University; 1999.
[15] Yamamoto Y, Nakamura H, Kuroda I, Furuya N. Analysis of compression failure of concrete by three-dimensional rigid body spring model. Doboku Gakkai Ronbunshuu 2008;64(4):612–30 [in Japanese].
[16] Yamamoto Y. Evaluation of failure behaviors under static and dynamic loadings of concrete members with mesoscopic scale modeling. PhD thesis. Nagoya, Nagoya University; 2010 [In Japanese].
[17] Walraven J, Lehwalter N. Size effects in short beams loaded in shear. ACI Struct J 1994;91(5):585–93.
[18] Zhang N, Tan KH. Size effect in RC deep beams: experimental investigation and STM verification. Eng Struct 2007;29:3241–54.
[19] Tan KH, Cheng GH. Size effect on shear strength of deep beams: investigating with strut-and-tie model. J Struct Eng ASCE 2006;132(5):673–85.
[20] Bazant ZP, Kazemi MT. Size effect on diagonal shear failure of beams without stirrups. ACI Struct J 1991;88(3):268–76.
[21] Kotsovos MD, Pavlovic MN. Size effects in beams with small shear span-to-depth ratios. Comput Struct 2004;82:143–56.
[22] Gedik YH, Nakamura H, Yamamoto Y, Kunieda M. Analyses of pre- and post-peak behavior of deep beams failed in shear using 3-D-RBSM. In: Oh BH,

editor. Proceedings of the 7th international conference on fracture mechanics of concrete and concrete structures; 2010. p. 493–500.
[23] Nagai K, Sato Y, Ueda T. Mesoscopic simulation of failure of mortar and concrete by 3D RBSM. J Adv Concr Technol, JCI 2005;3(3):385–402.
[24] Saito S, Hikosaka H. Numerical analysis of reinforced concrete structures using spring network model. Journal of Materials, Concrete Structures and Pavements, JSCE 1999;44(627):289–303.
[25] Suga M, Nakamura H, Higai T, Saito S. Effect of bond properties on the mechanical behavior of RC beam. Proc Japan Concrete Inst 2001;23(3): 295–300 [in Japanese].
[26] Comite Euro-International du Beton. CEB-FIB model code 1990 first draft. CEB, Paris; 1990.
[27] Cornelissen HAW, Hordijk DA, Reinhardt HW. In: Wittann FH, editor. Experiments and theory for the application of fracture mechanics to normal and lightweight concrete, fracture toughness and fracture energy of concrete. Elsevier; 1986. p. 565–75.
[28] Fujikake K, Shinozaki Y, Ohno T, Mizuno J, Suzuki A. Post-peak and strain-softening behaviors of concrete materials in compression under rapid loading. J Mater, Concr Struct Pavements 1998;44(627):37–54 [in Japanese].
[29] Kostovos MD, Newman JB. Generalized stress–strain relations for concrete model. J Eng Mech, ASCE 1978;125:845–56.
[30] Akiyama M, Hong KN, Sato M, Suzuki M, Maeda N, Suzuki M. Effect of transverse reinforcement on behavior of high strength concrete columns under concentric compression and its modeling of stress–strain relationship. Journal of Materials, Concrete Structures and Pavements 2004;753(5–62):137–51 [in Japanese].